



Effect of thermal expansion on thermal contact resistance prediction based on the dual-iterative thermal–mechanical coupling method



Yan-Jun Dai^a, Xing-Jie Ren^a, Yun-gang Wang^a, Qi Xiao^{b,*}, Wen-Quan Tao^{a,*}

^a Key Laboratory of Thermo-Fluid Science and Engineering of MOE, School of Energy and Power Engineering, Xi'an Jiaotong University, Xi'an, Shaanxi, 710049, P.R. China

^b Science and Technology on Thermal Energy and Power Laboratory, Wuhan, Hubei, 430205, P.R. China

ARTICLE INFO

Article history:

Received 24 August 2020

Revised 15 March 2021

Accepted 18 March 2021

Available online 1 April 2021

Keyword:

Numerical prediction

Thermal expansion

Thermal contact resistance

Dual-iterative coupling method (DICM)

Single sequential coupling method (SSCM)

ABSTRACT

This study investigates the effect of thermal expansion on thermal contact resistance prediction, proposing a dual-iterative coupling method (DICM). The contact surfaces in the simulation model are reconstructed based on either the actual measured topography or the hypothetical topography, and a mathematical formulation for numerically predicting the thermal contact resistance (TCR) is established. The DICM includes four steps: first, mechanical analysis is conducted based on the ideal single point contact condition, according to the elastic–plastic constitutive equations. Second, heat transfer analysis is carried out based on the deformed geometry originating from the prior mechanical analysis. Third, another step of mechanical analysis is implemented to consider the effect of thermal expansion with the temperature distribution determined in the second step. Fourth, another step of heat transfer analysis is carried out based on the deformed geometry originating from the second-step mechanical analysis. The conventional prediction method only contains the first and second steps, and is known as the single sequential coupling method (SSCM). The TCRs of two engineering examples are predicted using both DICM and SSCM. The results show that the mechanical–thermal–mechanical–thermal dual-iterative coupling method, i.e., DICM, should be recommended for simulating contact pairs with axisymmetric geometries, while SSCM is suggested for contact pairs with non-axisymmetric geometry.

© 2021 Elsevier Ltd. All rights reserved.

1. Introduction

Surface–surface contact is ubiquitous between components in engineering systems, which inevitably introduces thermal contact resistance (TCR) when heat transfer takes place. The TCR at high temperatures requires significant research for hypersonic aircrafts [1] and nuclear reactors [2]. The research approaches for TCR can be primarily divided into theoretical analyses [3,4], numerical simulations [5,6], and experimental studies [7–9]. For example, theoretical analyses and numerical simulations are frequently used to study pellet-cladding thermal–mechanical interactions (PCIs), which induce large stresses in the cladding, and could lead to fuel rod failure. In both theoretical analyses and numerical simulations, three key steps are usually followed [10]. For theoretical analyses, surface-topography generation, contact-deformation determination, and establishment of a single asperity or multi-asperity ther-

mal contact-resistance model must be accomplished. For instance, Zhang et al. [11] proposed an analytical model for TCR in which the rough surfaces are characterized using the 3D Weierstrass–Mandelbrot (W-M) fractal function. Three deformation modes are analyzed—elastic, elastic–plastic, —and the classical Cooper–Mikic–Yovanovich (CMY) model [12], based on single idealized contact, is adopted to obtain the expression for the TCR. Jackson et al. [13] developed a multiscale model that considers the multiple scales of surface roughness and the scale dependence of the mechanical and thermal properties based on Archard's [14] theoretical model. These theoretical models have significant limitations in terms of their applicability for arbitrary mechanical roughness. Further, in numerical simulations, surface-topography generation, contact-deformation analysis, and heat transfer calculations are the three key steps to follow [15]. For surface-topography generation, the statistical model [16], the fractal model [17,18], and the measured practical rough topography [19] have been adopted in previous studies. The practical rough surface model established from measurements can significantly mitigate the uncertainty of topography assumptions originating from statistical and fractal models.

* Corresponding authors.

E-mail addresses: zhiyan7@sina.com (Q. Xiao), wqtao@mail.xjtu.edu.cn (W.-Q. Tao).

In terms of the numerical methods, the finite element method (FEM) [14,18–20], finite volume method (FVM) [21], the finite difference method (FDM) [22], and the lattice Boltzmann method (LBM) [23,24], are typically used to predict the TCR. The LBM used to predict TCR operates from a mesoscopic perspective, resulting in a limited computational size. The FDM employed to simulate TCR also has limitations in terms of simulating complex surface structures; therefore, there has not been much research on this topic. The FVM inherently satisfies the criterion of energy conservation irrespective of its mesh size; however, the deformation process cannot be resolved easily using this method. TCR has been well-researched in the field of thermal–mechanical coupling; therefore, the FEM is often regarded as the most suitable method to predict TCR in engineering applications. For example, Thompson [19] implemented the FEM to solve the thermal/structural problem in the micro- and macro-scales by implementing iterations with each other. Murashov and Panin [20] adopted the FEM to simulate the contact heat transfer problem of hardened rough surfaces based on the fractal model.

Even though so much papers were published related to numerical prediction of TCR, only a limited papers were published that actually predicted the TCR by implementing the mechanical and thermal analyses on the discretized grids. For example, Gou and Dai et al. [10,15] adopted the single sequential coupling method (SSCM) for TCR prediction with FEM. In their research, one mechanical simulation that neglects thermal expansion followed by one thermal simulation is implemented. To the best of our knowledge, there are no previous studies that consider the effect of thermal expansion on TCR prediction. However, for some specific situations, the mechanical and thermal effects are closely related when determining TCR, necessitating complete thermal–mechanical coupling for solutions. If a complete thermal–mechanical coupling simulation is used, it will become very difficult to obtain convergent numerical solutions and the computing time will become very high. Therefore, one more sequential solution after the first sequential solution is proposed in this paper, which is termed as the dual-iterative coupling method (DICM). The superiority of the DICM is that the effect of thermal expansion can be considered in the second mechanical analysis and the deformation due to thermal expansion can be calculated. Subsequently, the heat transfer due to mechanical deformation and thermal deformation can both be calculated in the second heat transfer analysis.

In this paper, the DICM for TCR prediction is proposed, and the effects of thermal expansion on TCR prediction have been thoroughly investigated in two engineering applications. The rest of the paper is organized as follows. The governing equations for the DICM are presented in Section 2. The boundary conditions of two practical engineering applications are provided in Section 3. Section 4 presents the details of the predicted results for the two examples. Finally, some conclusions are drawn in Section 5.

2. Governing equations

To consider the effects of thermal expansion, the DICM is adopted. There are a total of four calculation steps involved in the DICM. The first step is mechanical analysis, which is governed by the elastic–plastic constitutive equations based on the ideal single point contact condition. The second step is heat transfer analysis based on the deformed geometry originating from the first mechanical analysis. The third step is a second round of mechanical analysis that considers the effect of thermal expansion with the predicted temperature distribution. The fourth step is a second round of heat transfer analysis based on the deformed geometry determined from the second mechanical analysis. The governing equations for DICM are as follows.

2.1. Mechanical analysis

The stress–strain governing equations that consider the effect of thermal expansion for the elastic stage and plastic stage are documented in literature [25,26] and are simply showed as follows.

For the elastic stage:

$$\begin{aligned}\varepsilon_x &= \frac{1}{E}[\sigma_x - \mu(\sigma_y + \sigma_z)] + \alpha_T \Delta T \\ \varepsilon_y &= \frac{1}{E}[\sigma_y - \mu(\sigma_x + \sigma_z)] + \alpha_T \Delta T \\ \varepsilon_z &= \frac{1}{E}[\sigma_z - \mu(\sigma_y + \sigma_x)] + \alpha_T \Delta T \\ \gamma_{xy} &= \frac{1}{G} \tau_{xy}, \gamma_{yz} = \frac{1}{G} \tau_{yz}, \gamma_{zx} = \frac{1}{G} \tau_{zx}\end{aligned}\quad (1)$$

For the plastic stage:

$$\begin{aligned}d\varepsilon_x &= \frac{1}{2G} ds_x + d\lambda s_x + \alpha_T dT, d\gamma_{xy} = \frac{1}{G} d\tau_{xy} + d\lambda \tau_{xy} \\ d\varepsilon_y &= \frac{1}{2G} ds_y + d\lambda s_y + \alpha_T dT, d\gamma_{yz} = \frac{1}{G} d\tau_{yz} + d\lambda \tau_{yz} \\ d\varepsilon_z &= \frac{1}{2G} ds_z + d\lambda s_z + \alpha_T dT, d\gamma_{zx} = \frac{1}{G} d\tau_{zx} + d\lambda \tau_{zx}\end{aligned}\quad (2)$$

where σ_i ($i = x, y, z$) and ds_i ($i = x, y, z$) are the normal stress; τ_{ij} ($ij = xy, yz, xz$) and $d\tau_{ij}$ ($ij = xy, yz, xz$) are the shear stress; ε_i ($i = x, y, z$) and $d\varepsilon_i$ ($i = x, y, z$) are the normal strain; γ_{ij} ($ij = xy, yz, xz$) and $d\gamma_{ij}$ ($ij = xy, yz, xz$) are the shear strain, $G = \frac{E}{2(1+\mu)}$, where E and μ are the Young's modulus and the Poisson's ratio, respectively; and G is the shear modulus. $d\lambda = \frac{3d\varepsilon_i}{2\sigma_i}$. α_T is the thermal expansion coefficient, and ΔT and dT is the temperature difference in difference and differential form respectively. In this study, the property parameters are considered to be temperature-dependent.

The differences of the stress–strain governing equations between the first step and the third step are only the thermal expansion term showed in Eqs. (1) and (2). The governing equations of the first step are also well documented in literature [25,26] and will not be restated here for simplicity.

2.2. Heat transfer analysis

The heat transfer between two contact surfaces with the interstitial gap consists of three parts: (a) conduction through the actual contact spots of two solids; (b) conduction through the interstitial gap; (c) radiation heat transfer between the two surfaces of gaps.

The governing equation of heat conduction in bodies is well documented in literature [27]. The radiative heat transfer in gaps is governed by the classic Stefan–Boltzmann radiation equation which is described detailed in literature [15]. Xu et al. found that, when the gap distance is larger than the dominant wavelength, λ_{th} , of the thermal radiation, where λ_{th} is defined using Wien's displacement rule [28], the thermal radiation between two interfaces can be also calculated by the Stefan–Boltzmann law. In this study, the distances between two solid surfaces are of the order of tens of microns, which is much larger than the characteristic wavelength determined by Wien's rule (about 6 microns at the lowest temperature of 500 K in this paper). In the study [15], it was found that the maximum difference—with or without considering radiation in the air gap—is 2.17% when the two contact surfaces are near 400°C. This implies that the effect of radiation on TCR is limited. Thus even if the calculation of radiation heat transfer is not

accurate, say the emissivity of the material surface is roughly estimated, the effect on TCR prediction is very limited.

Equations of heat conduction across the gaps and the gap conductance determination can also refer to literature [15]. As indicated above the gap distances in this study are about tens of microns, and much larger than the gas mean free path; therefore, the continuous model is still valid.

3. Boundary conditions

Boundary conditions are usually related to specific problems that need to be specified. In this paper, two engineering applications will be used as examples. To facilitate a comparison of the results, the same problems are analyzed using both DICM and SSCM.

3.1. TCR model between thermal protection layers

A multilayer thermal protection system (TPS, including TC4, ultra-high temperature ceramics, aerogels, phase change materials, etc.) is designed for hypersonic aircraft to sustain the large temperature difference between the outer surface and inner space owing to severe aerodynamic heating. The multilayers in this paper do not refer to the thin-coating protection layers on the surface of the material. TCR will always exist between two adjacent layers, which is a crucial consideration in the thermal design of multilayer TPS. The underestimation of the TCR will lead to an excessive thickness of the thermal protection structure, increasing the TPS weight, which should be minimized for hypersonic aircraft. Therefore, TCR is an important factor in the design of TPS for the weight-constrained hypersonic aircraft. Furthermore, the precise prediction of TCR between thermal protection layers has become a limitation (others include the melting point, chemical stability, thermal conductivity, etc.) that affects the reliability of TPS.

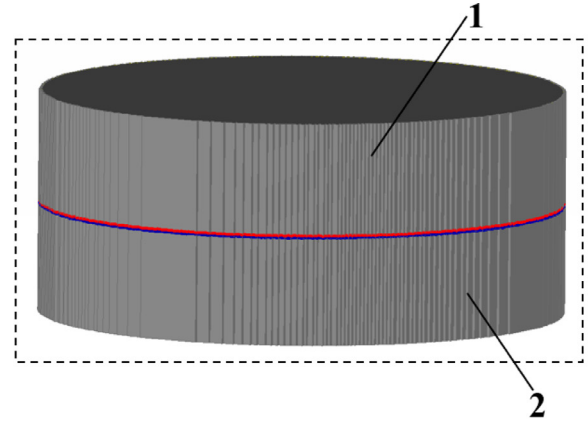
In this paper, the TC4–TC4 contact pair is selected as the TPS material to investigate the effects of thermal expansion on TCR prediction. Fig. 1(a) shows the computational model of the TC4–TC4 (1-2) contact pair. The upper TC4(1) and lower TC4(2) are both 48 mm in diameter and 8 mm in height, so the total computational domain dimensions are 48 mm in diameter and 16 mm in height. The boundary conditions for the mechanical and heat transfer analysis are shown in Fig. 1 (b), and can be defined as follows:

First step, mechanical analysis [15]:

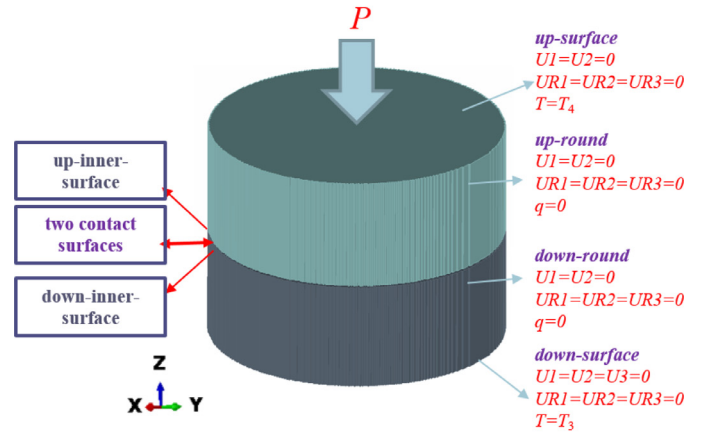
$$\begin{aligned} \text{Up - surface: } & \begin{cases} U_1 = U_2 = 0 \\ P = P_0; \end{cases} \\ \text{Up - round: } & \begin{cases} U_1 = U_2 = 0 \\ UR_1 = UR_2 = UR_3 = 0; \end{cases} \\ \text{Down - surface: } & \begin{cases} U_1 = U_2 = U_3 = 0 \\ UR_1 = UR_2 = UR_3 = 0; \end{cases} \\ \text{Down - round: } & \begin{cases} U_1 = U_2 = 0 \\ UR_1 = UR_2 = UR_3 = 0; \end{cases} \end{aligned} \quad (3)$$

Second step, heat transfer analysis[15]:

$$\begin{aligned} \text{Up - surface: } & T = T_4; \\ \text{Up - round: } & q = 0; \\ \text{Down - surface: } & T = T_3; \\ \text{Down - round: } & q = 0; \end{aligned} \quad (4)$$



(a) Computational domain



(b) Boundary conditions

Fig. 1. Computational domain and boundary conditions of TPS [15].

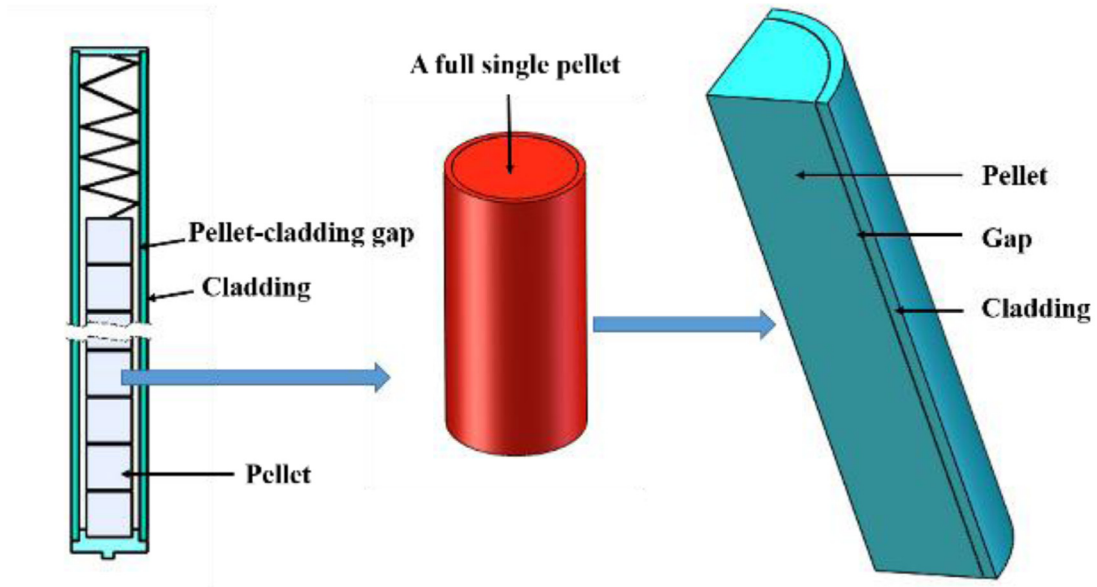
Third step, mechanical analysis:

$$\begin{aligned} \text{Up - surface: } & \begin{cases} U_1 = U_2 = 0 \\ P = P_0; \end{cases} \\ \text{Up - round: } & \begin{cases} U_1 = U_2 = 0 \\ UR_1 = UR_2 = UR_3 = 0; \end{cases} \\ \text{Down - surface: } & \begin{cases} U_1 = U_2 = U_3 = 0 \\ UR_1 = UR_2 = UR_3 = 0; \end{cases} \\ \text{Down - round: } & \begin{cases} U_1 = U_2 = 0 \\ UR_1 = UR_2 = UR_3 = 0; \end{cases} \end{aligned} \quad (5)$$

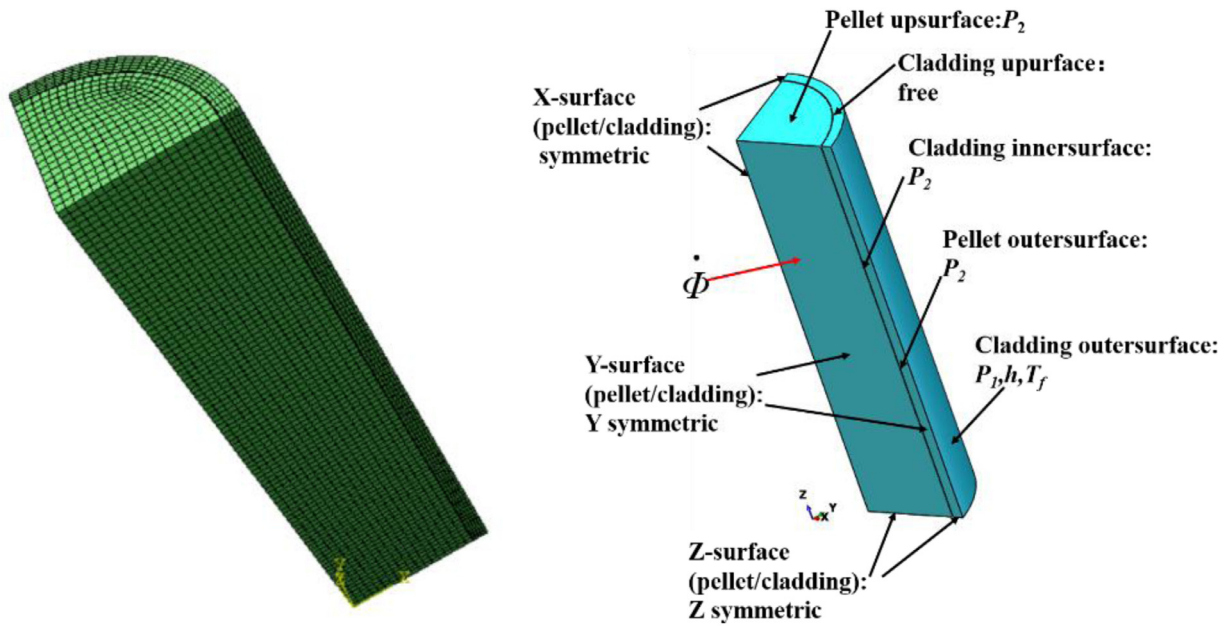
Whole model: $T = T_{2\text{nd step}}$

Fourth step, heat transfer analysis:

$$\begin{aligned} \text{Up - surface: } & T = T_4; \\ \text{Up - round: } & q = 0; \\ \text{Down - surface: } & T = T_3; \\ \text{Down - round: } & q = 0; \end{aligned} \quad (6)$$



(a) Schematic and computational model



(b) Boundary conditions

Fig. 2. Numerical model and boundary conditions of pellet and cladding.

where U_1 , U_2 , and U_3 denote the displacement in the x , y , and z directions respectively; UR_1 , UR_2 , and UR_3 denote the rotation displacement in the three spatial angles, respectively; P_0 denotes the actual pressure on the up-surface (4.65MPa); T_3 (243.9°C) and T_4 (183.8°C) denote the actual temperature on the up-surface and down-surface; and $T_{2nd\ step}$ denotes the temperature distribution

results obtained from the second step of the analysis. The material properties are listed in Table 1.

The finite element analysis of the mechanical and heat transfer performance of the contact surfaces is implemented using ABAQUS, based on the topology of the measured surface. The specimen surface topography is measured using a microscope (Bruker Contour

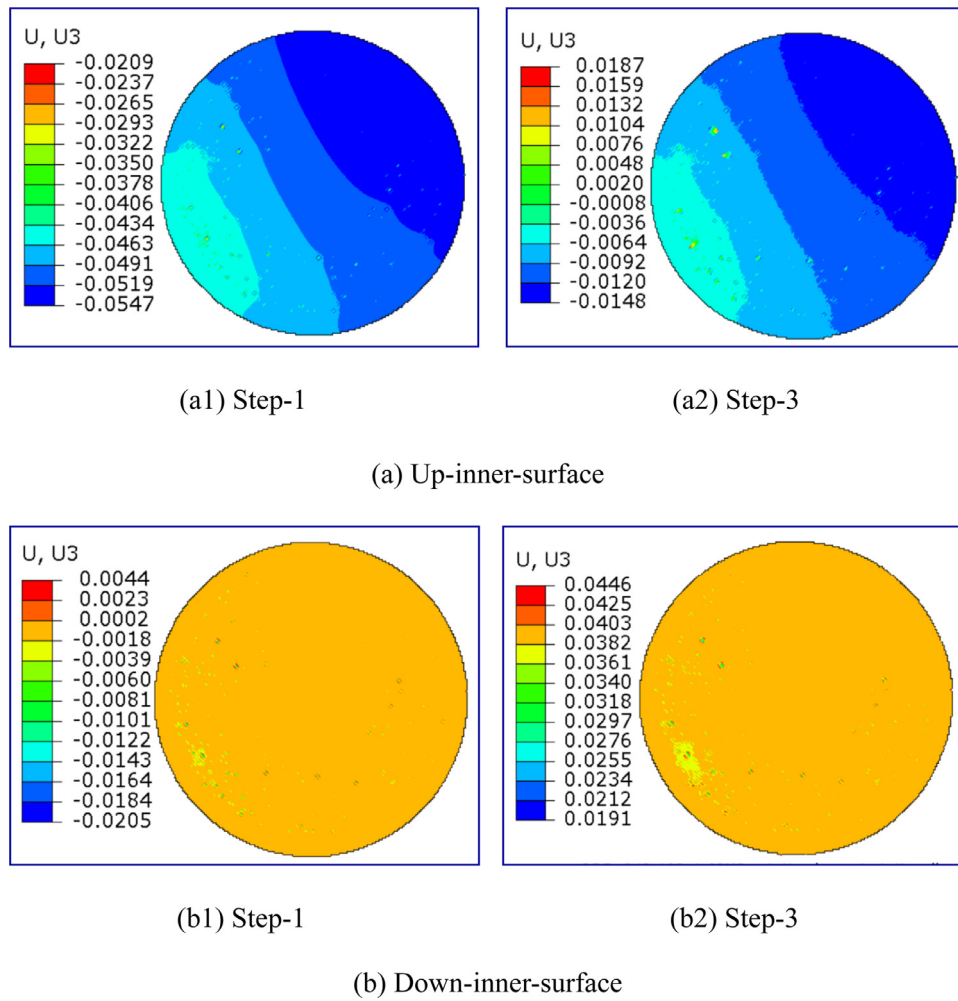


Fig. 3. Displacement distribution of up-inner-surface and down-inner-surface.

Table 1
Ti-6Al-4V properties at different temperatures [15].

T/(°C)	Young's Modulus/ (GPa)	Poisson's ratio	Expansion coefficient × 10 ⁶	Yield strength/ (MPa)	Plastic strain	Thermal conductivity/ (W/m-K)
20	120.59	0.286	7.882			6.8
100	120.05	0.284	8.53			7.4
200	115.5	0.294	9.34	860	0	8.7
300	113.39	0.299	9.52			9.8
400	108.1	0.314	9.79	980.6	0.1	10.3
500	92.98	0.352	9.83			11.8

GT-K) with a vertical resolution of 0.1 nm. The average surface roughness of the up-inner-surface and down-inner-surface are 11.3 μm and 19.7 μm, respectively. The contact-surface reconstruction process and the computational model establishment process are as follows. Based on the measured surface's topography, the two contact surface roughnesses are reconstructed within every four neighboring points in the coons-surfaces style of ABAQUS. Further, the data for every eight adjacent measured points are used as the nodes to generate one element. A very small horizontal movement of one surface is implemented to ensure that there is only one contact point of the two contact surfaces. This ideal single contact point is set up as the initial contact condition for the simulation analysis. A mesh with 1,778,432 hexahedral elements and 1,858,890 nodes is applied to implement the numerical analysis. The emissivity of TC4 is 0.6.

It is important to note that this study considers the TCR in the macroscale, i.e., the thermal boundary resistance (also known as interfacial thermal resistance or Kapitza resistance) is not taken into account. The reason is that the surface roughness in this study is of the order of tens of microns, which is much larger than the nano or atomic scale. Therefore, the boundary thermal resistance caused by phonon scattering at the interface can be neglected [29,30].

3.2. TCR model between a pellet and cladding

The second TCR model investigated in this paper is that for the TCR between a pellet and cladding in nuclear engineering. When designing the fuel bundle of a pressurized water reactor (PWR), a certain gap is assumed to exist between the outer surface of the

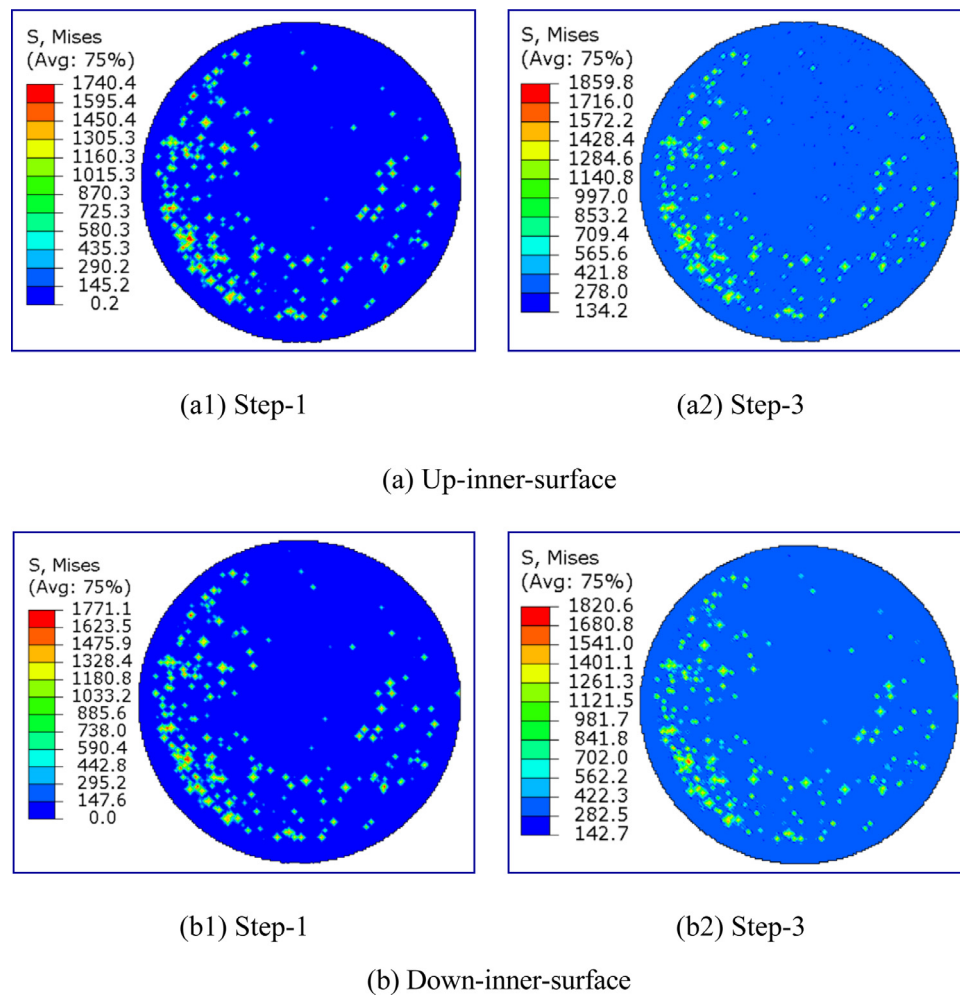


Fig. 4. Mises stress distribution of up-inner-surface and down-inner-surface.

fuel pellet and the inner surface of the cladding [31–33]. The gap is initially filled by low molecular weight helium. A very narrow gap can result in significant temperature distribution changes in the fuel pellet. Therefore, the reliability of gap-conductance prediction is crucial to ensure the safety of PWRs. Gap conductance depends on the burnup and can be divided into two main stages: gap conduction at the initial stage of low burnup and contact conduction at the subsequent stage of high burnup. With the increases in burnup, the expansion caused by temperature rises, and cracks and swelling occur owing to the irradiation of the fuel pellets. Further, the creep of the cladding and release of fission gas occur simultaneously. These aforementioned factors may cause the pellets to come into contact with the cladding. In this study, as a first approximation, only the effect of expansion on contact conduction is considered in detail, while other factors are not taken into account.

Fig. 2(a) shows the schematic and computational model for the pellet–cladding (1-2) contact pair. 1/8 of a full single pellet is selected as the computational model because of its symmetry. The radius and the height of the pellet are 4.3 mm and 20 mm, respectively. The thickness of the cladding is 0.5 mm. The topographies of the outer surface of the pellet and inner surface of cladding are generated artificially. The average surface roughnesses of the outer surface of the pellet and inner surface of the cladding are 7.52 μm and 7.54 μm, respectively [34]. Here, the ideal single contact point is also set up as the initial contact status for the simulation analysis. Meshes with 44,800 hexahedral elements and 52,015 nodes are

applied to implement the numerical analysis of the computational model.

The fuel pellet acts as a volumetric heat source and the coolant transfers heat away through the outer surface of the cladding. The boundary conditions for the mechanical and heat transfer analysis are shown in Fig. 2(b) and can be defined as follows:

First step, mechanical analysis:

$$\text{Pellet upsurface: } P = P_2;$$

$$\text{Cladding innersurface: } P = P_2;$$

$$\text{Pellet outersurface: } P = P_2;$$

$$\text{Cladding outersurface: } P = P_1;$$

(7)

$$\text{X - surface(pellet/cladding): } U_1 = UR_2 = UR_3 = 0;$$

$$\text{Y - surface(pellet/cladding): } U_2 = UR_1 = UR_3 = 0;$$

$$\text{Z - surface(pellet/cladding): } U_3 = UR_1 = UR_2 = 0;$$

Second step, heat transfer analysis:

$$\text{Pellet: } q = \dot{\Phi};$$

Table 2
Pellet (UO₂) properties at different temperatures.

T/(°C)	Young's Modulus/ (GPa)	Poisson's ratio	Expansion coefficient (10 ⁻⁶)	Yield strength/(MPa)	Plastic strain	Yield strength/(MPa)	Plastic strain	Thermal conductivity/(W/m•K)
300	189.730	0.316	8.85329	538.90	0	578.50	0	5.45
400	187.510	0.316	9.14071	500.00	0	535.82	0.01	4.78
500	185.288	0.316	9.39743	461.09	0	493.14	0.01	4.26
600	183.067	0.316	9.63952	422.18	0	450.45	0.01	3.85
700	180.845	0.316	9.87351	383.28	0	407.76	0.01	3.51
800	178.624	0.316	10.1025	344.37	0	365.07	0.01	3.24
900	176.403	0.316	10.3283	305.47	0	322.38	0.01	3.01
1000	174.182	0.316	10.5518	266.56	0	279.69	0.01	2.83

4. Results and discussion

4.1. Comparison of the effects of thermal expansion for thermal protection layers

The mechanical results for displacement, von Mises stress, and the contact area are found and subsequently analyzed. Fig. 3(a) shows the U3/mm displacement (z-direction of the pressure exerted) distribution of the up-inner-surface from the first step and third step. Fig. 3(b) shows the distribution for the down-inner-surface from the first step and third step. It can be seen that the difference between the results of the first step and the third step is that the effect of thermal expansion is not considered in the first step and it is considered in the third step. For the up-inner-surface in the first step, the displacements of all nodes are downward, from -2.09×10^{-2} mm to -5.47×10^{-2} mm (with an average value of -5.0×10^{-2} mm), as the computational model is subjected to the downward pressure P . For the down-inner-surface in the first step, a majority of the displacement is also downward, while several individual spots exhibit upward deflection owing to deformation, from -2.05×10^{-2} mm to 4.4×10^{-3} mm, with an average of -3.0×10^{-4} mm. It is clear that the displacement value of the up-inner-surface is obviously larger than that of the down-inner-surface. For the up-inner-surface in the third step, the displacements of all nodes are from -1.0×10^{-2} mm to 1.87×10^{-2} mm, with an average value of -1.48×10^{-2} mm. It can be seen that the displacements of several spots turn upward and the average displacement becomes smaller because of the expansion effect. For the down-inner-surface in the third step, the displacements of all nodes are from 1.91×10^{-2} mm to 4.46×10^{-2} mm, with an average value of 3.95×10^{-2} mm. It can be observed that the displacement of the entire surface turns upward because of expansion. Figs. 4(a), (b) show the von Mises stress distribution of the up-inner-surface and down-inner-surface, respectively. The von Mises stress distribution and values of the two contact surfaces from the two steps are approximately the same. In Fig. 4(a), the maximum von Mises stresses from step 1 and step 3 are 1740 MPa and 1859 MPa, respectively. They are larger than the yield stress—860 MPa—which implies that the deformation of some elements enters the plastic stage. Therefore, it is necessary to consider plasticity in the mechanical simulation. Figs. 5(a), (b) show the contact area distributions of the up-inner-surface and down-inner-surface, respectively. The bright spots denote the real contact area. In the blue to red labels in Figs. 5(a), (b), the real contact areas of the elements vary from 0 to 6.63×10^{-2} (6.65×10^{-2}) mm². The percentage of the real contact area per unit nominal area from the first and the third steps are both 1.03%.

Next, the heat transfer results for temperature and heat flux are presented and discussed. Figs. 6, 7 represent the temperature distribution of the lateral wall, up-inner-surface and down-inner-surface from the second step and fourth step. In Fig. 6, the difference between lateral temperature results from the second step

$$\text{Cladding outersurface: } -\lambda \frac{\partial T}{\partial n} = h(T - T_f); \quad (8)$$

Third step, mechanical analysis:

$$\text{Pellet upsurface: } P = P_2;$$

$$\text{Cladding innersurface: } P = P_2;$$

$$\text{Pellet outersurface: } P = P_2;$$

$$\text{Cladding outersurface: } P = P_1; \quad (9)$$

$$X - \text{surface(pellet/cladding): } U_1 = UR_2 = UR_3 = 0;$$

$$Y - \text{surface(pellet/cladding): } U_2 = UR_1 = UR_3 = 0;$$

$$Z - \text{surface(pellet/cladding): } U_3 = UR_1 = UR_2 = 0;$$

$$\text{Whole model: } T = T_{2\text{nd step}}$$

Fourth step, heat transfer analysis:

$$\text{Pellet: } q = \dot{\Phi};$$

$$\text{Cladding outersurface: } -\lambda \frac{\partial T}{\partial n} = h(T - T_f); \quad (10)$$

where U_1 , U_2 , and U_3 denote the displacement in the x , y , and z directions, respectively; UR_1 , UR_2 , and UR_3 denote the rotation displacement in the three spatial angles, respectively; P_2 denotes the helium pressure in the gap (4.5 MPa); P_1 denotes the coolant pressure flow through the outer surface of the cladding (15.5 MPa); $\dot{\Phi}$ denotes the volumetric heat source (320.4 mW/mm³); λ is the thermal conductivity of the cladding; $\frac{\partial T}{\partial n}$ is the temperature gradient; h is the heat transfer coefficient (20000W/m²·K); T_f is the coolant temperature (300°C); and $T_{2\text{nd step}}$ denotes the temperature-distribution results obtained from the second step of the analysis. The emissivities of the pellet and cladding are 0.871 and 0.809 [35], respectively. The material properties of pellet and cladding are listed in Table 2 and Table 3, respectively [34].

Table 3
Cladding (Zircaloy) properties at different temperatures.

T/(°C)	Young's Modulus/(GPa)	Poisson's ratio	Expansion coefficient(10 ⁻⁶)	Yield strength/(MPa)	Plastic strain	Yield strength/(MPa)	Plastic strain	Thermal conductivity/(W/m•K)
300	80.408	0.355	4.35747	244.31	0	252.35	0.01	16.17
320	79.296	0.357	4.36269	240.14	0	248.07	0.01	16.41
340	78.184	0.359	4.36729	235.96	0	243.78	0.01	16.64
360	77.072	0.360	4.37139	231.79	0	239.50	0.01	16.88
380	75.961	0.362	4.37505	227.61	0	235.21	0.01	17.11
400	74.849	0.364	4.37835	223.44	0	230.92	0.01	17.35

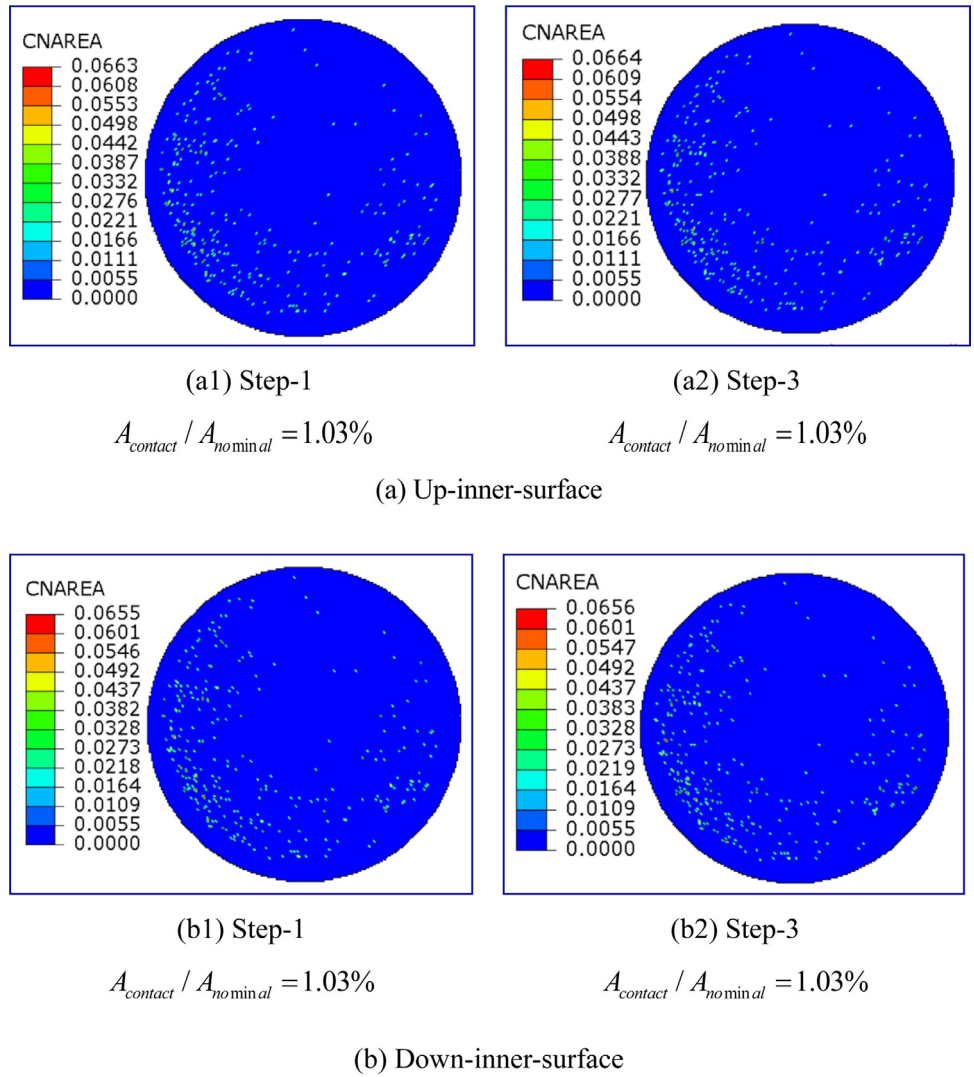


Fig. 5. Contact area distribution of up-inner-surface and down-inner-surface.

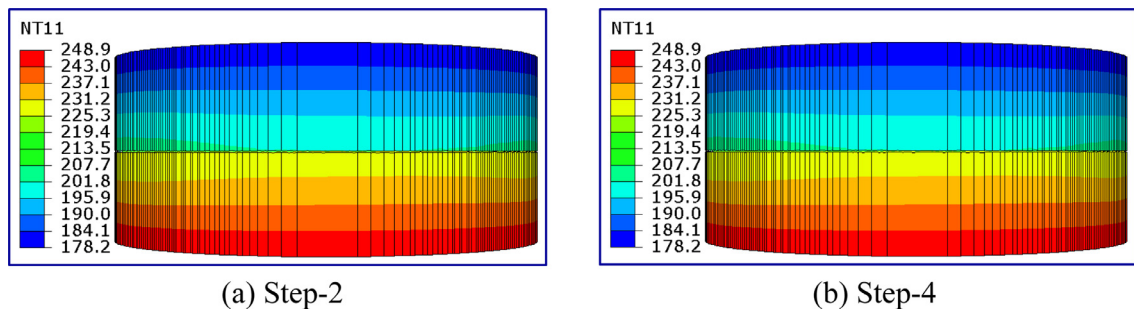


Fig. 6. Lateral wall temperature distribution of the 1st model.

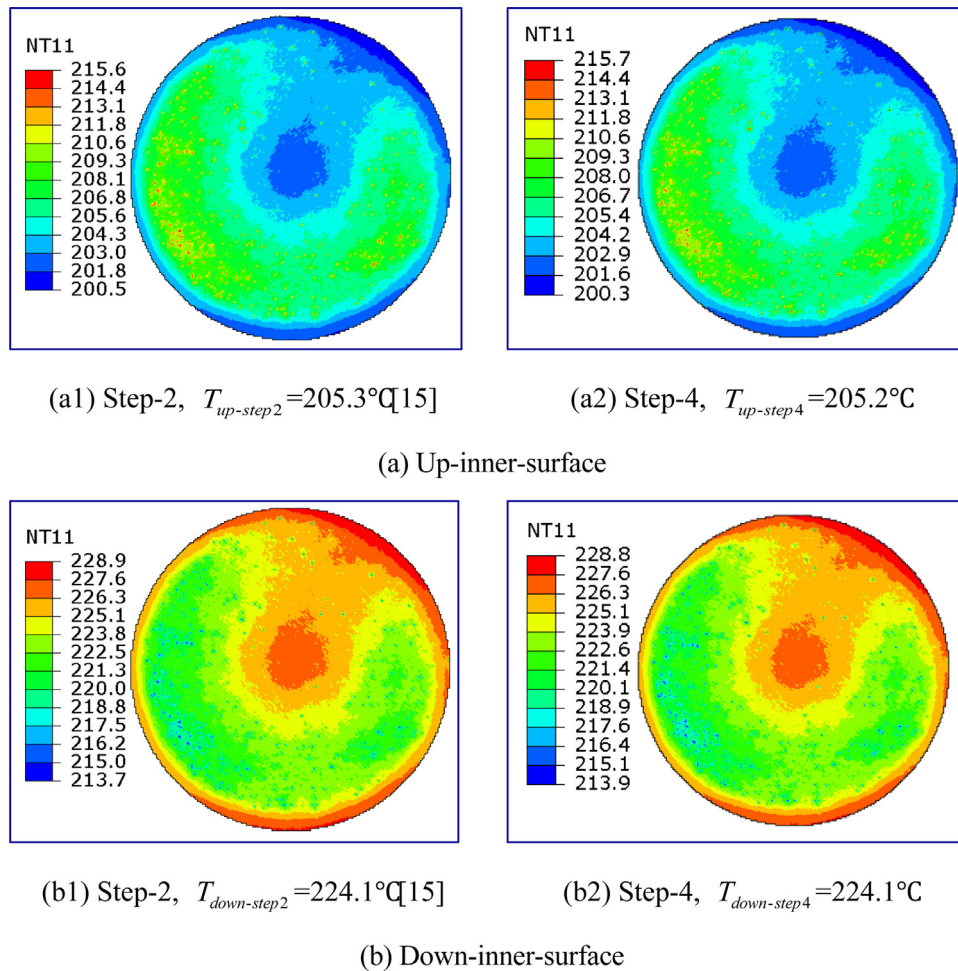


Fig. 7. Temperature distribution of up-inner-surface and down-inner-surface from the 1st example.

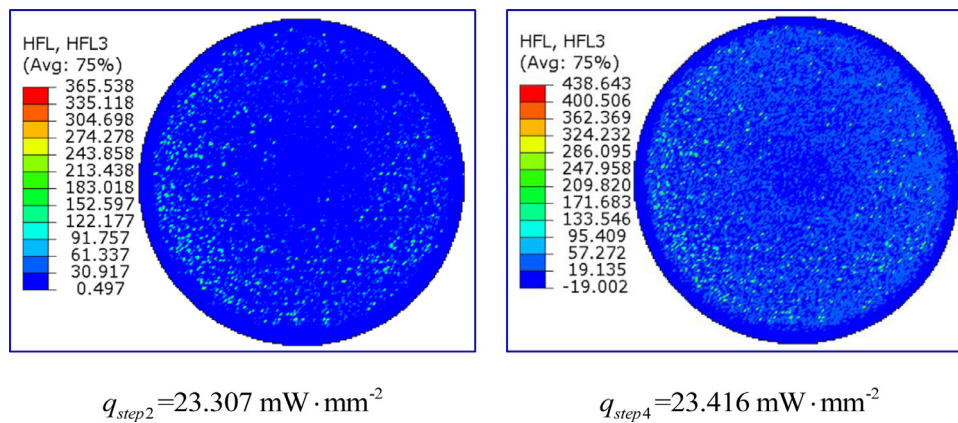


Fig. 8. Heat flux distribution of up-inner-surface.

and the fourth step is whether the thermal expansion effect is not considered or considered. The temperature is in °C unit. It is found that the temperature distributions are identical within one digit after the decimal, irrespective of thermal expansion. However, the average temperatures of the up-inner-surface show a little difference between Step 2 and Step 4, which are 205.3 °C and 205.2 °C in the two steps, respectively, as shown by Fig. 7 (a), but the average temperatures of the down-inner-surface for Step 2 and Step 4 are both 224.1 °C. The heat-flux distributions from the second and

fourth steps are given in Fig. 8, in $\text{mW} \cdot \text{mm}^{-2}$. The average heat flux from the second step is $q_{step2} = 23.307 \text{ mW} \cdot \text{mm}^{-2}$, while that from the fourth step is $q_{step4} = 23.416 \text{ mW} \cdot \text{mm}^{-2}$, with a deviation of 0.46%. A careful observation on Fig. 7(a) and (b) can find that in Step 4 there are more spots in the center part of the test section have an appreciable local heat flux. However, because of their very small local area, the averaged surface flux only increased by 0.46%.

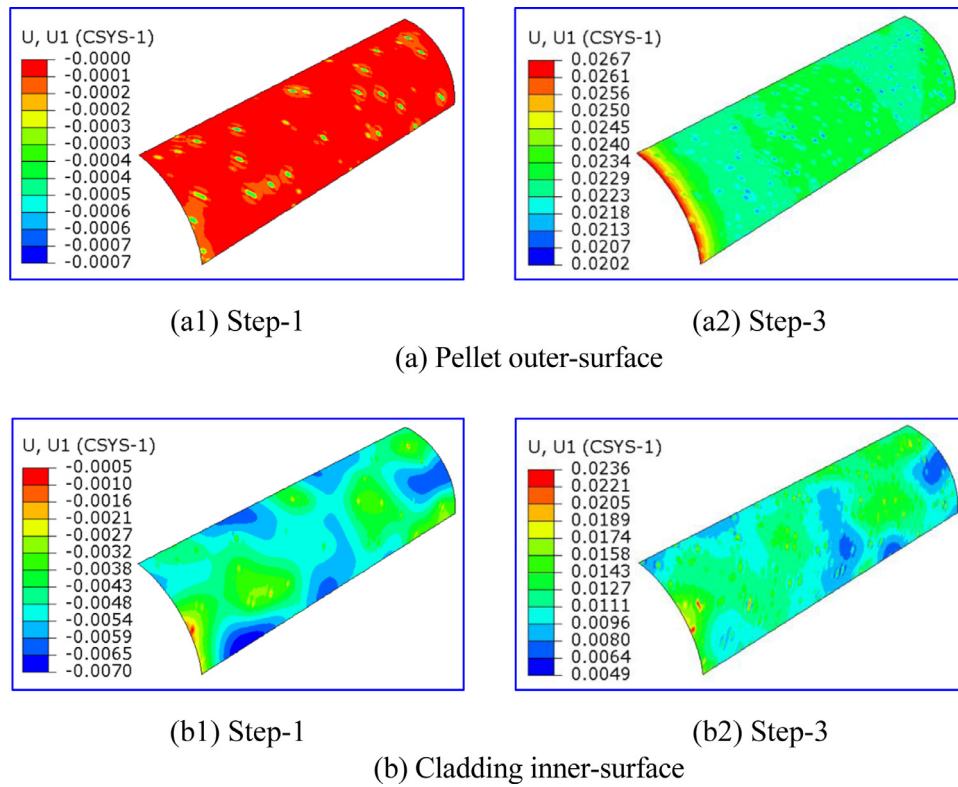


Fig. 9. Displacement distribution of pellet outer-surface and cladding inner-surface.

The thermal contact resistance, TCR, is defined as:

$$TCR = \frac{\Delta T}{q} = \frac{T_{down} - T_{up}}{q} \quad (11)$$

where T_{down} and T_{up} are the average temperature of the down-inner-surface and up-inner-surface, respectively. These two contact surface's average temperatures are calculated from the arithmetic average temperature of all nodes on the contact surfaces. ΔT is the temperature difference between T_{down} and T_{up} . q is the average heat flux in the axial direction flowing through the contact surfaces. The two TCR values are:

$$TCR_{step2} = \frac{\Delta T}{\bar{q}} = \frac{T_{down-step2} - T_{up-step2}}{\bar{q}_{step2}} = \frac{224.1 - 205.3}{23307} = 8.066 \times 10^{-4} \text{C} \cdot \text{m}^2 \cdot \text{K}^{-1} \quad (12)$$

$$TCR_{step4} = \frac{\Delta T}{\bar{q}} = \frac{T_{down-step4} - T_{up-step4}}{\bar{q}_{step4}} = \frac{224.1 - 205.2}{23416} = 8.071 \times 10^{-4} \text{C} \cdot \text{m}^2 \cdot \text{K}^{-1} \quad (13)$$

The experimental result is $7.75 \times 10^{-4} \text{C} \cdot \text{m}^2 \cdot \text{K}^{-1}$ from the 1D steady platform [15] under the same boundary conditions, and the deviation is 4% for the TCR from the second step. The deviation of TCR from the two steps is only 0.06%, which implies that the effects of thermal expansion need not be considered in the prediction, and that SSIM can adequately simulate the TCR for the investigated thermal protection system.

4.2. Comparison of the effects of thermal expansion for the pellet and cladding model

First, the mechanical results for displacement, von Mises stress, and the contact area are presented and discussed. Figs. 9, 10 show the displacement and von Mises stress distributions of the pellet

outer-surface and cladding inner-surface from the first step and third step, respectively. U1/mm denotes the radial direction of the exerted pressure. In the first step, the displacements of the pellet outer-surface and the cladding inner-surface are negative when the pressure is exerted. For the pellet outer-surface in the first step, the maximum displacement is -7.24×10^{-4} mm, while the minimum displacement is -3.88×10^{-5} mm, with an average value of -7.93×10^{-5} mm. For the cladding inner-surface in the first step, the maximum displacement is -7.04×10^{-3} mm, while the minimum displacement is -4.69×10^{-4} mm, with an average value of -4.83×10^{-3} mm. It is clear that the displacement value of the cladding inner-surface is obviously larger than that of the pellet outer-surface. For the pellet outer-surface in the third step, the maximum displacement is 2.67×10^{-2} mm, while the minimum displacement is 2.02×10^{-2} mm, with an average value of 2.30×10^{-2} mm. For the cladding inner-surface in the third step, the maximum displacement is 2.36×10^{-2} mm, while the minimum displacement is 4.9×10^{-3} mm, with an average value of 1.13×10^{-2} mm. For the third step, the displacement of the two contact surfaces turns positive owing to the effects of expansion, while the displacement of the pellet outer-surface is larger than that of the cladding inner-surface. Figs. 11(a), (b) show the contact-area distributions of the pellet outer-surface and the cladding inner-surface, respectively. The percentage of the real contact area per unit nominal area from the third step is approximately 9.38%, which is almost five times of the value from the first step, 1.91%. Therefore, it is clear that the von Mises stress distribution differs for the two steps. In Figs.9 to 11, the differences between Steps 1 and 3 are so appreciable, only major quantitative results are presented, and no detail comparisons are made for the simplicity of presentation.

Next, the results for the temperature and heat flux are presented and discussed. Figs. 12, 13 represent the temperature distribution of the entire model, and the two surfaces (pellet outer-surface and cladding inner-surface), respectively, from the second

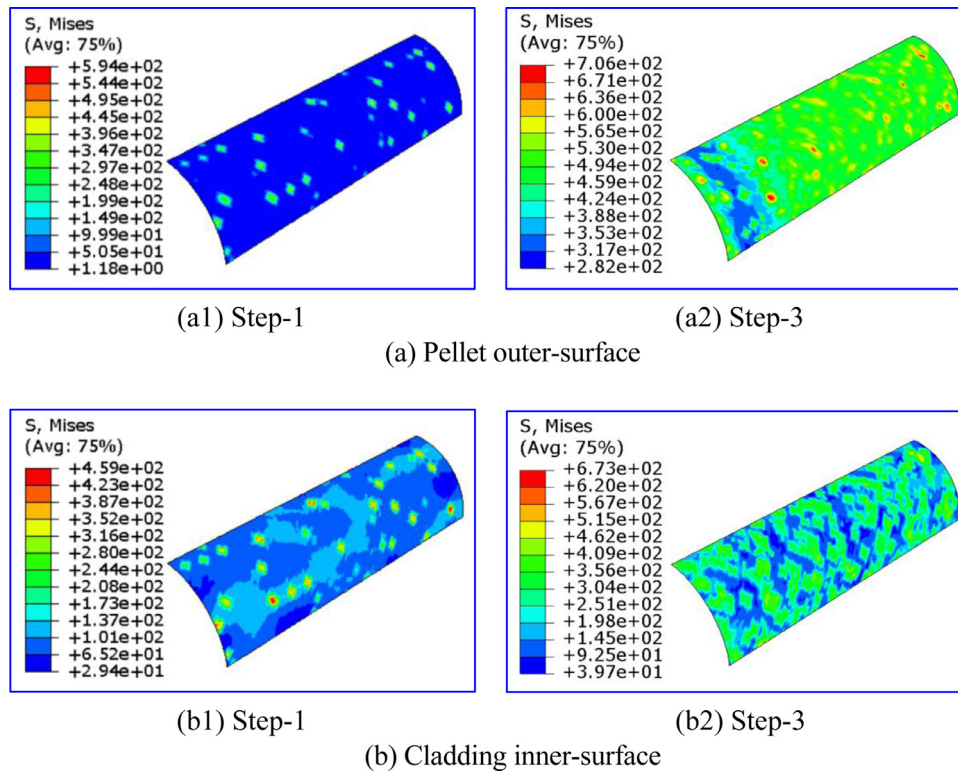


Fig. 10. Mises stress distribution of pellet outer-surface and cladding inner-surface.

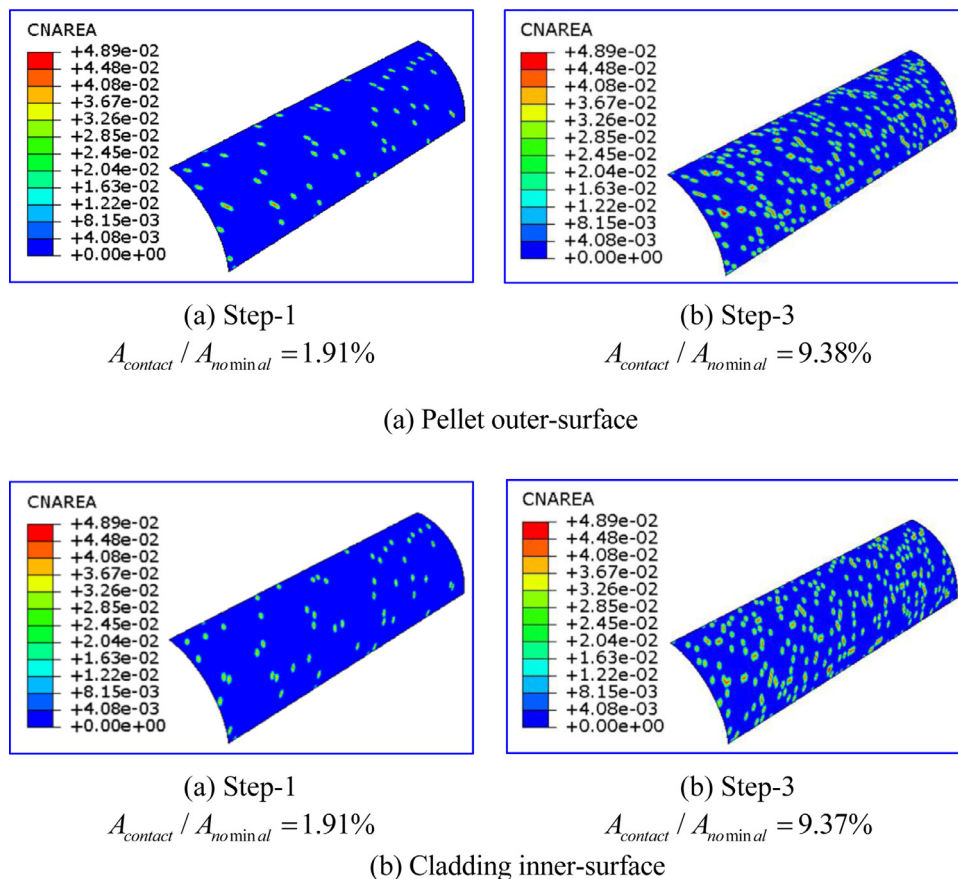


Fig. 11. Contact area distribution of pellet outer-surface and cladding inner-surface.

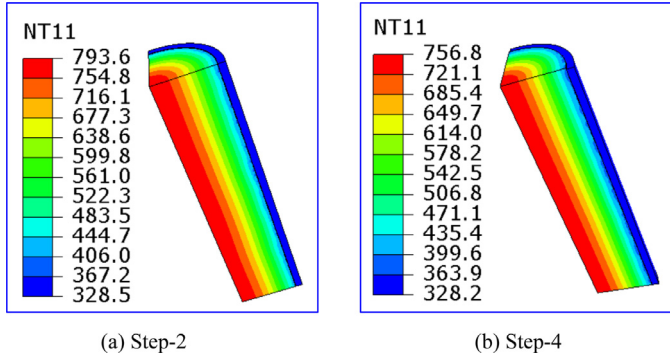


Fig. 12. Whole model temperature distribution of the 2nd example.

step and fourth step. It is to be noted that even though the qualitative pictures of Fig. 12(a) and (b) are almost the same, the temperature scales of the two figures are different, with the up-scale of Fig. 12(b) being about 37 °C lower than that of Fig. 12(a). The temperature of the central axis from the fourth step is about 36.8 °C higher than that from the second step. The average temperatures of the pellet outer-surface are 409.5°C and 382.1°C for the two steps, respectively, which indicates that more heat transfers from the pellet to the cladding when the real contact area increases owing to the effects of thermal expansion in the fourth step. The average temperatures of the cladding inner-surface for the two steps, 350.3 °C and 350.9 °C, respectively, are nearly the same. This is because the high heat transfer rate to the cladding can be mitigated by the high coolant heat transfer coefficient, 20000W/m² · K. The heat flux radial component distribution of the pellet outer-surface from the second step and fourth step are

given in Figs. 14(a), (b), respectively. The heat flux radial component distribution of the cladding inner-surface from the second step and fourth step are shown in Figs. 15 (a), (b), respectively. The radial heat flux of the pellet outer-surface from the second step is $q_{p-o-step2} = 692.512 \text{ mW} \cdot \text{mm}^{-2}$, while that from the fourth step is $q_{p-o-step4} = 694.268 \text{ mW} \cdot \text{mm}^{-2}$. Further, the radial heat flux of the cladding outer-surface from the second step is $q_{c-i-step2} = 688.063 \text{ mW} \cdot \text{mm}^{-2}$, while that from the fourth step is $q_{c-i-step4} = 698.398 \text{ mW} \cdot \text{mm}^{-2}$. It can be seen that, despite the real contact area increasing, the average heat flux is almost the same for the two steps, with a deviation less than 1.48%.

The thermal contact resistance, TCR, is determined by an equation similar to Eq. (11).

$$TCR = \frac{\Delta T}{q} = \frac{T_{p-o} - T_{c-i}}{q} \quad (14)$$

where T_{p-o} and T_{c-i} are the average temperatures of the pellet outer-surface and cladding inner-surface shown in Fig. 13, respectively. ΔT is the temperature difference between T_{p-o} and T_{c-i} , and q is the average radial heat flux that flows through the contact surfaces. The values of the two TCRs are as follows:

$$TCR_{step2} = \frac{\Delta T}{\bar{q}} = \frac{T_{p-o-step2} - T_{c-i-step2}}{\bar{q}_{step2}} = \frac{409.5 - 350.3}{\frac{692512 + 688063}{2}} = 8.576 \times 10^{-5} \text{ } ^\circ\text{C} \cdot \text{m}^2 \cdot \text{K}^{-1} \quad (15)$$

$$TCR_{step4} = \frac{\Delta T}{\bar{q}} = \frac{T_{p-o-step4} - T_{c-i-step4}}{\bar{q}_{step4}} = \frac{382.1 - 350.9}{\frac{694268 + 698398}{2}} = 4.481 \times 10^{-5} \text{ } ^\circ\text{C} \cdot \text{m}^2 \cdot \text{K}^{-1} \quad (16)$$

The deviation of the TCR in the two steps is as high as 91.4%, which implies that the effects of thermal expansion must be con-

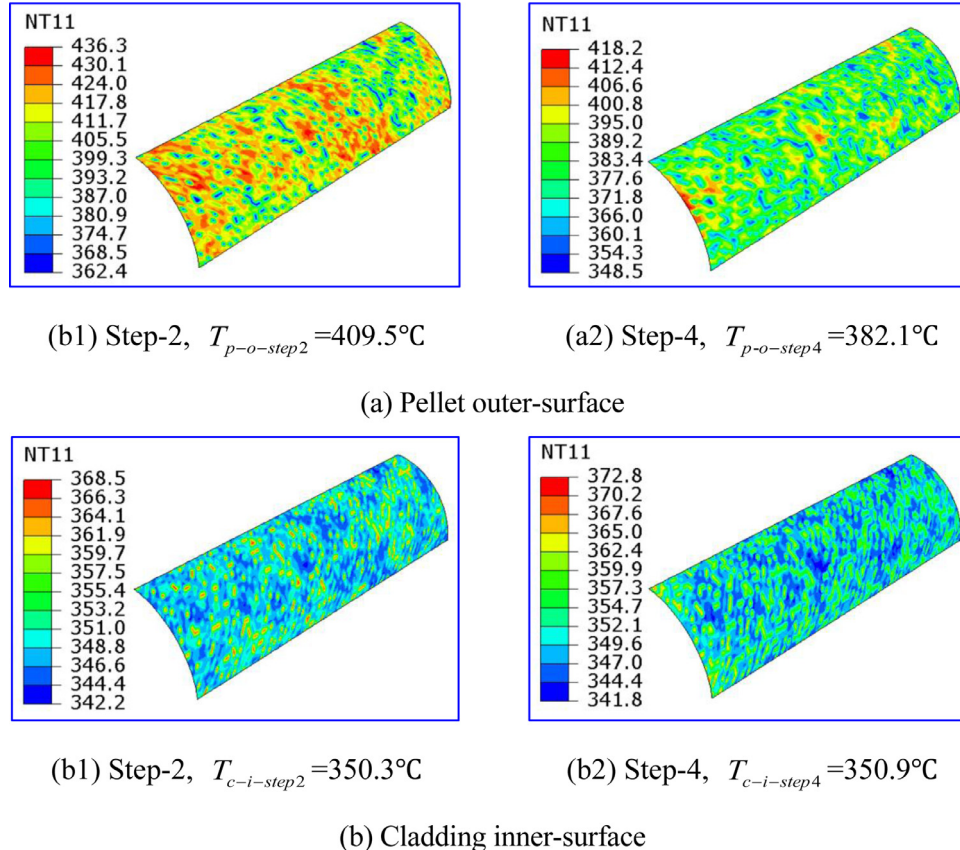


Fig. 13. Temperature distribution of pellet outer-surface and cladding inner-surface.

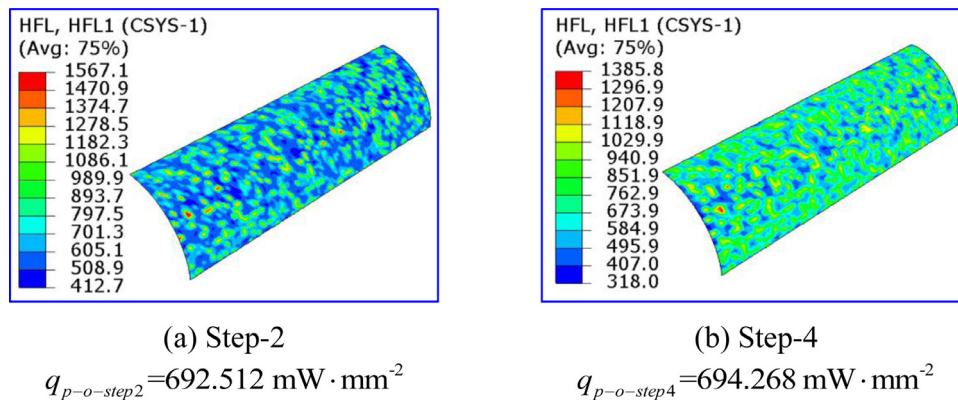


Fig. 14. Heat flux radial component distribution of pellet outer-surface.

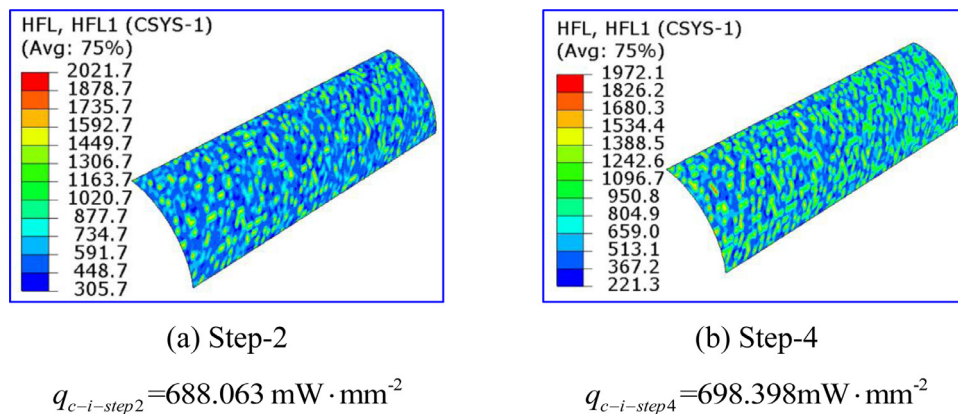


Fig. 15. Heat flux radial component distribution of cladding inner-surface.

sidered in the prediction; DICM must be adopted to simulate the TCR between the pellet and cladding.

Come here a question may arise as why we do not conduct iteration deeply by using SSCM so that the effect of thermal expansion can be considered? As indicated in Introduction, a complete thermal-mechanical coupling simulation is very difficult to obtain convergent numerical solutions because of highly non-linearity, and the solution process usually is of segregated type, as presented in this paper by the DICM. And this is a usually approach in numerical community when a highly non-linear problem is to be numerically solved. Then it is clear that in the SSCM, no matter how deep the iteration is conducted, the thermal expansion effect could not be taken into account. Only DICM can take the effect of thermal expansion into account.

As indicated above, in nuclear engineering, determining the TCR is of great importance, and significant uncertainty still exists in this field at present. The prediction equations for determining TCR under the same conditions can differ by 10 times in their results [36,37]. This indicates that further research, both experimental and numerical, is of great importance to improve the prediction accuracy of TCR; the present paper makes a contribution in this regard.

Further, it is important to note that, in the first example, the surface roughness is measured, while in the second example, it is artificially generated. Different roughnesses will lead to differing results for TCR. However, for a given roughness, the predicted TCR should not be affected by the way the roughness is obtained, whether it is experimentally measured or artificially generated.

4.3. Differences between the two cases

The TCR values for the first example predicted by SSCM and DICM are almost the same, while those for the second example differ appreciably. It is important to note that the Young's Modulus, thermal expansion characteristics of the materials, and the implemented pressure of the two examples are similar. To exclude the influence of the physical properties on the TCR results, a comparative simulation is conducted by substituting the pellet's physical properties for the cladding's. The real contact area percentages of the pellet outer surface from the first step and third step are 0.62% and 8.60%, respectively, as shown in Fig. 16. It can be seen that the differences in the real contact areas of the two cases are roughly the same (8.6% and 0.62% versus 9.38% and 1.91%). The authors believe that these differences mainly arise from different models' structures. For the second example, with axisymmetric geometry, the radial displacements will be partially mutually suppressed when the radial pressure is implemented and the average radial displacements of cladding inner-surface and pellet outer-surface in the first step are only -4.83×10^{-3} mm and -7.93×10^{-5} mm, respectively. For the first example, with the fixed down-surface, the average displacements of the up-inner-surface and down-inner-surface in the first step are as large as -5.0×10^{-2} mm and -3.0×10^{-4} mm, respectively.

For the first example, the average displacements of the two surfaces in the third step are -1.48×10^{-2} mm and 3.95×10^{-2} mm, respectively. The average gap distances of the ideal contact status, first step, and third step are 102.22 μ m, 52.50 μ m, and 52.80

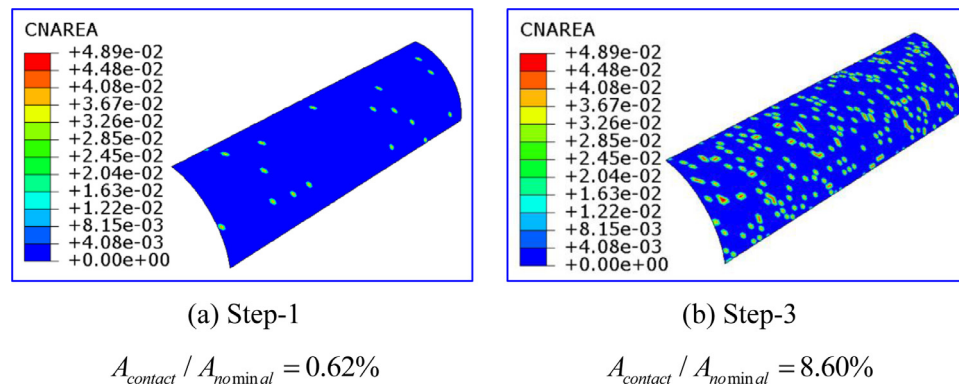


Fig. 16. Contact area distribution of pellet outer-surface with the same physical properties.

μm , respectively. With the increases in the implemented pressure, the gap distance decreases from $102.22 \mu\text{m}$ to $52.50 \mu\text{m}$. Further, the gap distance from the first step and third step is almost the same, which leads to the same percentage of real contact area and the same TCR. For the second example, the average displacements of the two surfaces in the third step are $1.13 \times 10^{-2} \text{ mm}$ and $2.30 \times 10^{-2} \text{ mm}$, respectively. The gap distances of the ideal contact status, first step, and third step are $29.46 \mu\text{m}$, $24.70 \mu\text{m}$, and $18.4 \mu\text{m}$, respectively. The gap distance decreases from $29.46 \mu\text{m}$ to $24.70 \mu\text{m}$ with increases in the implemented pressure on the contact pairs. Further, the gap distance decreases from $24.70 \mu\text{m}$ to $18.4 \mu\text{m}$ as the thermal expansion is taken into account in the third step, which leads to a larger percentage of real contact area and larger TCR. From the above discussion, it can be concluded that DICM should be recommended for contact pairs with axisymmetric geometry, while SSCM is suggested for contact pairs with non-axisymmetric geometry.

5. Conclusion

In this paper, the dual-iterative coupling method (DICM) for predicting TCR is proposed, which focuses on the effects of thermal expansion on TCR prediction. The TCRs of thermal protection layers and of pellets and claddings are considered as practical engineering examples; both the DICM and the conventional single sequential coupling method (SSCM) are adopted for predicting their values. The predicted results and their differences are discussed in detail. The major conclusions can be summarized as follows:

(1) For the thermal protection layers studied, the average gap distances of the first step and third step are $52.50 \mu\text{m}$ and $52.80 \mu\text{m}$ under the pressure of 4.65 MPa . Further, the percentage of the real contact area per unit nominal area from the first and the third steps are both 1.03%. The same gap distance leads to the same percentage of real contact area and the same TCR about $8.1 \times 10^{-4} \text{ }^\circ\text{C} \cdot \text{m}^2 \cdot \text{K}^{-1}$, even though the effects of thermal expansion are taken into account, indicating that one step of mechanical analysis and one heat transfer analysis (SSCM) are sufficiently accurate in predicting the TCR.

(2) For the TCR of the pellet and cladding, the gap distance decreases from $24.70 \mu\text{m}$ to $18.4 \mu\text{m}$ as the thermal expansion is taken into account in the third step. Further, the percentage of the real contact area per unit nominal area from the third step is approximately 9.38%, which is five times that of the first step, 1.9%. The values of the two TCRs are $8.576 \times 10^{-5} \text{ }^\circ\text{C} \cdot \text{m}^2 \cdot \text{K}^{-1}$ and $4.481 \times 10^{-5} \text{ }^\circ\text{C} \cdot \text{m}^2 \cdot \text{K}^{-1}$. The deviation of TCR from the two steps can get as high as 91.4%, which implies that the effects of thermal expansion must be considered in the prediction and the DICM, i.e., two mechanical and two heat transfer analyses must be adopted to simulate the TCR between the pellet and the cladding.

(3) For all TCR simulation models for practical engineering, DICM must be used for contact pairs with axisymmetric geometry, and the SSCM method will lead to great errors owing to the neglect of thermal expansion effect.

Credit author statement

Wen-Quan Tao: Conceptualization, Methodology, Resources, Writing-Review & Editing; **Qi Xiao:** Supervision, Project administration, Funding acquisition; **Yan-Jun Dai:** Methodology, Software, Validation, Formal analysis, Investigation, Data Curation, Writing-Original Draft, Visualization; **Xing-Jie Ren:** Investigation; **Yun-gang Wang:** Writing - Review & Editing

Declaration of Competing Interest

We wish to confirm that there are no known conflicts of interest associated with this publication and there has been no significant financial support for this work that could have influenced its outcome.

We confirm that the manuscript has been read and approved by all named authors and that there are no other persons who satisfied the criteria for authorship but are not listed. We further confirm that the order of authors listed in the manuscript has been approved by all of us. We confirm that we have given due consideration to the protection of intellectual property associated with this work and that there are no impediments to publication, including the timing of publication, with respect to intellectual property. In so doing we confirm that we have followed the regulations of our institutions concerning intellectual property.

We understand that the Corresponding Author is the sole contact for the Editorial process (including Editorial Manager and direct communications with the office). He is responsible for communicating with the other authors about progress, submissions of revisions and final approval of proofs. We confirm that we have provided a current, correct email address which is accessible by the Corresponding Author and which has been configured to accept email from wqtao@mail.xjtu.edu.cn

Acknowledgements

This work is supported by the National Natural Science Foundation of China (No. 51806167), China Postdoctoral Science Foundation (2017M623166), Science and Technology on Thermal Energy and Power Laboratory Open Foundation of China (No. TPL2017BA004), and 111 Project (B16038)

References

- [1] Y.J. Xu, N.X. Xu, W.H. Zhang, et al., A multi-layer integrated thermal protection system with C/SiC composite and Ti alloy lattice sandwich, *Composite Structures* 230 (2019) 111507.
- [2] N. Marchal, C. Campos, C. Garnier, Finite element simulation of Pellet-Cladding Interaction (PCI) in nuclear fuel rods, *Computational Materials Science* 45 (2009) 821–826.
- [3] M.A. Lambert, L.S. Fletcher, Review of models for thermal contact conductance of metals, *J. Thermo. Heat Transf.* 11 (2) (1997) 129–140.
- [4] M. Bahrami, J.R. Culham, M.M. Yovanovich, Thermal contact resistance of non-conforming rough surfaces, part 2: Thermal model, *J. Thermo. Heat Transf.* 18 (2) (2004) 218–227.
- [5] B. Salti, N. Laraqi, 3-D numerical modeling of heat transfer between two sliding bodies: temperature and thermal contact resistance, *Int. J. Heat Mass Transf.* 42 (13) (1999) 2363–2374.
- [6] D.H. Liu, J. Zhang, Numerical simulation of high-temperature thermal contact resistance and its reduction mechanism, *Plos One* 13 (3) (2018) e0194483.
- [7] R.P. Xu, L. Xu, An experimental investigation of thermal contact conductance of stainless steel at low temperatures, *Cryogenics* 45 (10-11) (2005) 694–704.
- [8] R.F. Dou, T.R. Ge, X.L. Liu, Effects of contact pressure, interface temperature, and surface roughness on thermal contact conductance between stainless steel surfaces under atmosphere condition, *Int. J. Heat Mass Transf.* 94 (2016) 156–163.
- [9] D.H. Liu, Y. Luo, X.C. Shang, Experimental investigation of high temperature thermal contact resistance between high thermal conductivity C/C material and Inconel 600, *Int. J. Heat Mass Transf.* 80 (13) (2015) 407–410.
- [10] J.J. Gou, X.J. Ren, Y.J. Dai, et al., Study of thermal contact resistance of rough surfaces based on the practical topography, *Comput. Fluids* 164 (2016) 2–11.
- [11] J.H. Zhang, Y.L. Liu, Y. Ke, et al., A fractal model for predicting thermal contact conductance considering elasto-plastic deformation and base thermal resistances, *J. Mech. Sci. & Tech.* 33 (1) (2019) 475–484.
- [12] M.G. Cooper, B.B. Mikic, M.M. Yovanovich, Thermal contact conductance, *Int. J. Heat Mass Transf.* 12 (3) (1969) 279–300.
- [13] R.L. Jackson, S.H. Bhavnani, T.P. Ferguson, A multiscale model of thermal contact resistance between rough surfaces, *J. Heat Trans.* 130 (2008) 081301-1.
- [14] J.F. Archard, Elastic deformation and the laws of friction, *Proc. R. Soc. London A243* (1957) 190–205.
- [15] Y.J. Dai, J.J. Gou, X.J. Ren, et al., A test-validated prediction model of thermal contact resistance for Ti-6Al-4V alloy, *Appl. Energy* 228 (2018) 1601–1617.
- [16] V. Bakolas, Numerical generation of arbitrarily oriented non-gaussian three-dimensional rough surfaces, *Wear* 254 (5-6) (2003) 546–554.
- [17] M.Q. Zou, B.M. Yu, J.C. Cai, et al., Fractal model for thermal contact conductance, *ASME J Heat Transf.* 130 (10) (2008) 101301-1–101301-9.
- [18] L. Kogut, R.L. Jackson, A comparison of contact modeling utilizing statistical and fractal approaches, *ASME J. Tribol.* 128 (1) (2005) 213–217.
- [19] M.K. Thompson, A multi-scale iterative approach for finite element modelling of thermal contact resistance, Massachusetts Institute of Technology, Cambridge (MA, USA), 2007.
- [20] M.V. Murashov, S.D. Panin, Numerical modelling of contact heat transfer problem with work hardened rough surfaces, *Int. J. Heat Mass Transf.* 90 (2015) 72–80.
- [21] N. Verma, Development and demonstration of thermal contact conductance (TCC) models for contact between metallic surfaces, The Ohio State University, Columbus (Ohio, USA), 2019.
- [22] S.M.S. Wahid, Numerical analysis of heat flow in contact heat transfer, *Int. J. Heat Mass Transf.* 46 (24) (2003) 4751–4754.
- [23] T. Cui, Q. Li, Y. Xuan, et al., Multiscale simulation of thermal contact resistance in electronic packaging, *Int. J. Therm. Sci.* 83 (2014) 16–24.
- [24] W.Z. Fang, J.J. Gou, L. Chen, W.Q. Tao, A multi-block lattice Boltzmann method for the thermal contact resistance at the interface of two solids, *App. Ther. Engi.* 138 (2018) 122–132.
- [25] G.T. Yang, *Introduction to Elasticity and Plasticity*, 2nd edition, Tsinghua University Press, Beijing, 2004.
- [26] Z.L. Xu, *Elasticity*, 4th edition. Higher Education Press, Beijing, 2006.
- [27] W.Q. Tao, *Numerical Heat Transfer* (2001).
- [28] J.B. Xu, K. Lauger, R. Moller, et al., Heat transfer between two metallic surfaces at small distances, *J. App. Phys.* 76 (11) (1994) 7209–7216.
- [29] P. Zhang, P. Yuan, X. Jiang, et al., A theoretical review on interfacial thermal transport at the nanoscale, *Small* 14 (2) (2018) 1702769.
- [30] C.V. Madhusudana, *Thermal contact conductance (Second Edition)*, Springer, 2014.
- [31] Y.H. Jung, S.J. Baik, Investigation of pellet-clad mechanical interaction in failed spent PWR fuel, *Corr. Sci.&Tech. Korea* 18 (5) (2019) 175–181.
- [32] S.K. Seo, S.U. Lee, E.H. Lee, 3D finite element simulation of pellet-cladding mechanical interaction, *Trans. Korean Soc. Mech. Engi. A* 40 (5) (2016) 437–447.
- [33] U. Yutaka, S. Tomoyuki, A. Masaki, Thresholds for failure of high-burnup LWR fuels by Pellet Cladding mechanical interaction under reactivity-initiated accident conditions, *J. Nuc. Sci. & Tech.* 56(12) 1063–1072.
- [34] Y.J. Jiang, Y. Cui, Y.Z. Huo, S.R. Ding, Three-dimensional FE analysis of the thermal-mechanical behaviors in the nuclear fuel rods, *Ann. Nuc. Energy* 38 (2011) 2581–2593.
- [35] M. Suzuki, H. Saitou, Y. Udagawa, et al., Light water reactor fuel analysis code FEMAXI-7; model and structure, *JAEA-Data/Code* (2013) 005.
- [36] H.Y. Liao, Z.X. Wu, L.G. Liu, et al., Modification and update of FROBA-ROD code and its applications in fuel rod behavior analysis for PWRs, *Ann. Nuc. Energy* 133 (2019) 900–915.
- [37] H. Xia, Y.W. Wu, W.X. Tian, et al., Development of a thermo-mechanical coupling code based on an annular fuel sub-channel code, *Nuclear Engi. & Design* 355 (2019) 110284.